Michael Lublow* and Thomas Schedel-Niedrig*

Water Oxidation Catalysts from Waste Metal Resources: A Facile Metal-Organic Electrochemical Approach

Abstract: A fabrication route is presented by a novel metal-organic electrochemical approach, allowing facile preparation of electrocatalytic metal and metal oxide thin films from solid metals at room temperature: divalent transition metals such as iron, nickel and cobalt can be deposited as amorphous oxyhydroxide films. Among them, nickel- and cobalt-prepared samples are showing high activity as water oxidation catalysts in alkaline electrolytes. The applicability to waste metal material is exemplified using one of the most abundant waste metal alloys, i.e. steel: with a suitable multi-layer architecture, comprising, a large surface-area iron oxyhydroxide core-geometry and a steel-derived catalytic overlayer, the overpotential for oxygen evolution (at 10 mA cm^{-2}) could be improved to only 370 mV. Chemical analysis is provided to elucidate the reaction pathway, encompassing metal halogenation, formation of meta-stable metal-organic intermediates or direct electrochemical reduction, respectively. Structural peculiarities of the derived films are finally demonstrated upon development of a photoactive nickel oxyhydroxide/silicon junction realizing a photocurrent of 1 mA cm^{-2} at the thermodynamic potential for oxygen evolution and short-term stabilization in the range of several hours.

Keywords: Differential electrochemical mass spectroscopy (DEMS); Electrophoretic deposition; Elektron miscropscopy (SEM, TEM); Oxygen evolution reaction; (photo)-electrochemistry; Transition metal oxides; X-ray Photoelectron Spectroscopy (XPS).

*Corresponding authors: Michael Lublow, Technical University Berlin, Department of Chemistry, Straße des 17. Juni 124, 10623 Berlin, Germany, e-mail: drlublow@gmail.com; and **Thomas Schedel-Niedrig,** Helmholtz-Zentrum Berlin für Materialien und Energie GmbH, Institut für Angewandte Materialforschung (EM-IAM), Hahn-Meitner-Platz 1, 14109 Berlin, Germany, e-mail: schedel-niedrig@helmholtz-berlin.de

In a generalized approach for identification of earth-abundant materials for energy application, waste metal resources can assume a pivotal role for inexpensive and environmentally benign production of heterogeneous catalysts. Particularly the large number of transition metals, present in ferrous metal alloys, makes an approach towards catalyst production from waste metals appealing. In an appropriate oxidation state, these transition metals are beneficial in such diverse reactions as polymerization of alkenes, dehydration and dehydrogenation reactions of alcohols or water electrolysis for production of hydrogen [1–3]. Particularly in water electrolysis, transition metal oxides are the primary electrocatalytic material for the oxygen evolution reaction, i.e. one of the half-cell reactions of electrochemical water splitting [4–10]. Commercially available alkaline electrolysers employ, for instance, nickel- and cobalt-oxide activated anodes while polymer electrolyte membrane (PEM) systems, operating under acidic conditions, rely on the more expensive catalysts of iridium oxide (ruthenium oxide) and platinum [11–14]. These catalysts, usually fabricated from high-purity source materials, are known to cause a significant portion of the overall costs of electrolysers. As a consequence, successful competition with less expensive but CO_2-emitting technologies for hydrogen generation, which rely on fossil resources such as natural gas, oil and coal and are covering nearly 96% of industrial hydrogen production, is widely impeded. The use of cheap waste metals for the preparation of water oxidation electrocatalysts would therefore offer considerable reduction in investment and maintenance costs and could consequently facilitate large-scale application of water electrolysis, ideally coupled to CO_2 emission-free technologies such as wind or solar. It is a considerable challenge, however, to develop efficient electrodes from cheap source materials, i.e. waste metals, which usually lack purity or are provided as alloys, combining thereby active catalytic elements with less or non-active moieties. In the following, this challenge is addressed for the case of catalysts suitable for electrolysis of water in alkaline electrolytes. It will be shown that, firstly, solid metals can be transformed in a cost-effective way to electrocatalytic thin films and, secondly, abundant and low-purity metals are suitable resources to realize efficient water oxidation catalysts. Key to the preparation of these electrocatalytic thin films is the direct formation of metal iodides from a piece of solid metal in an organic solvent such as acetone and the subsequent formation of metal-organic complexes under cathodic electrodeposition conditions.

The metal oxyhydroxide preparation is performed with precursor solutions of Ni, Co, Fe and Cu iodides that were produced by immersion of metal sheets (Goodfellow Corp. USA, size 2 cm^2, purity >99.95%) into a mixture of acetone (10 mL) and iodine (crystal powder, 60 mg). Prior to immersion, the metal sheets were

rubbed by abrasive paper and rinsed in acetone in order to remove surface oxides. The solutions, containing the metal sheets, were stirred for 5 min in an ultrasonic bath at 37 kHz. The temperature increased during this treatment from room-temperature to about 35 °C. Before electrochemical deposition, the metal sheets were removed from the solutions and two electrodes were employed, one being an fluorinated tin oxide (FTO) coated glass slide (anode) and the other being the respective supporting cathode (FTO or n-type silicon) (see Figure 1 top left). After potential-controlled deposition for 5 min at −10 V vs. counter electrode (FTO), samples were rinsed by acetone to dissolve remnant iodine. Film formation was observed at the supporting electrode (the cathode) while the counter-electrode (the anode) did not show any modification. Sheets of industrial steel samples were subject to identical handling and preparation conditions. After electrodeposition
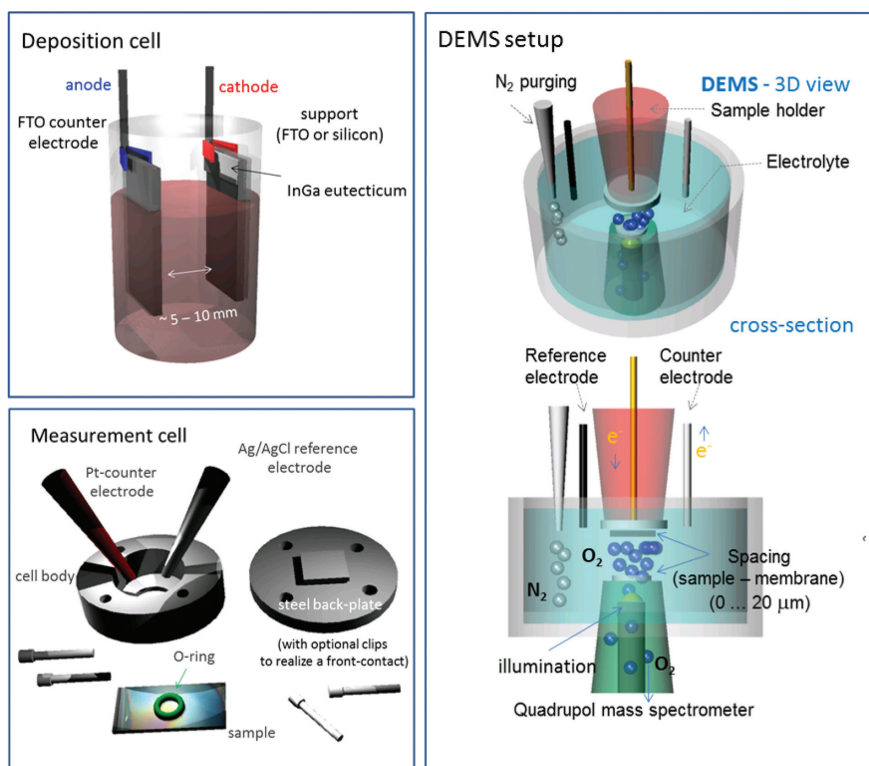
Fig. 1: Schematics of the used deposition cell, electrochemical cell and the setup for mass spectroscopic detection of evolving gases during electrochemical and, respectively, photoelectrochemical operation (DEMS).

and upon exposure to ambient air, immediate hydrolysis of these meta-stable complexes results in formation of a corresponding amorphous metal oxyhydroxide (MO_x) film. Recent investigations suggest that nickel oxide, enhanced by small quantities of iron oxide, reach best values in evolution of oxygen [5, 6, 10]. It should be mentioned that pure NiO_x actually exhibits very low activity in water electro-oxidation, unless tiny amounts of Fe^{3+} are present [5, 6].

One of the most abundant industrial metals, steel, on the other hand, typically comprises both elements but shows a much lower nickel to iron ratio than the aforementioned optimized Ni–Fe oxide electrodes. It will be shown, however, that surface activation of steel-derived electrodes, can significantly increase the number of active nickel oxide sites per geometrical surface area and thereby improve the kinetics of oxygen evolution towards reported best values. Thereby, efficiency in alkaline water oxidation is achieved at ultra-low costs and in a green-chemistry approach, i.e. with low CO_2-fingerprint. It is shown that the developed MO_x films are characterized by a dense morphologic structure which can positively influence their long-term stability. This finding is demonstrated by employing a NiO_x film as a catalytic protection layer on silicon, an oxidation-sensitive semiconductor. Thereby, a photoactive anode is realized, operating for hours without degradation, and realizing evolution of oxygen at the thermodynamic potential for water splitting (1.23 V vs. the reversible hydrogen electrode, RHE).

In the view of efficient evolution of oxygen in alkaline to near-neutral electrolytes, nickel and cobalt containing oxides are of highest efficiency [5, 6, 8, 10]. Accordingly, the electrocatalytic activity of nickel and cobalt oxyhydroxides was determined in model experiments using the corresponding ultra-pure solid metals. The results were subsequently compared to the activity of iron hydroxide and, finally, to a steel-derived electrode. As shown by the SEM-insets in Figure 2, the prepared films of nickel-, cobalt-and iron-derived MO_x films exhibit different surface morphologies, varying from pillar-like (nickel, iron) to lamella-like growth (cobalt). Investigation by X-ray diffractometry did not reveal any signals other than those of the FTO support, i.e. the films are fully amorphous. Good efficiency in oxygen evolution is achieved for nickel and cobalt oxyhydroxides: overpotentials of 0.43 V (NiO_x) and 0.42 V (CoO_x), respectively, were determined at current densities of 10 mA cm^{-2} for the IR potential drop corrected curves. The larger overpotential of 0.49 V in the case of FeO_x demonstrates lower activity of iron oxyhydroxide. Reversible Me(II) $\longrightarrow$ Me(III)/Me(II,III) transitions (Figure 2a and b) characterize the current-voltage curves for NiO_x and CoO_x. This feature is not observed with FeO_x (Figure 2c). Similar oxidation-reduction behavior was reported recently for amorphous NiO_x, CoO_x and FeO_x, prepared from metal-organic precursors and obtained after UV-light irradiation and annealing in air [15]. Film thicknesses range from about 200 nm (NiO_x and CoO_x) to about 5 mm
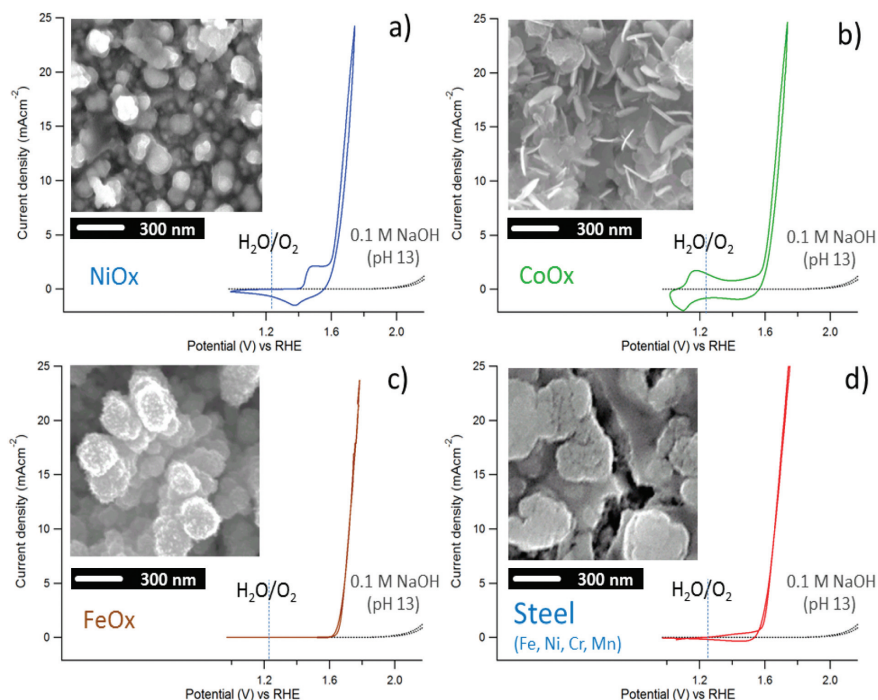
Fig. 2: Morphology and electrocatalytic properties of MO_x films on FTO, derived from solid sheets of nickel (a), cobalt (b), iron (c) and steel (d). Oxygen evolution was measured in 0.1 M NaO, pH13. Current densities were corrected for an uncompensated IR-drop determined by impedance spectroscopy. For comparison, the behavior of bare FTO is indicated as black curve in each graph. SEM images of the respective surfaces are shown as insets.

(FeO_x) after identical deposition times of 5 min. This pronounced difference in thickness is attributed to the higher rate of FeI_2 formation in the acetone/iodine solution in comparison to NiI_2 and CoI_2, respectively. In Figure 2d, corresponding results for an oxyhydroxide film obtained from a steel sample are shown. The used steel material contained about 9% Nickel and was subjected to identical deposition processes as for Ni, Co and Fe. The overpotential at 10 mA cm^{-2} of 0.43 V is comparable to NiO_x. Due to the low Ni concentration the reversible oxidation and reduction processes are much less pronounced than for pure NiO_x (compare Figure 2a and d). Nickel is considered to be mainly responsible for the good efficiency in evolution of oxygen for the steel-prepared film. A further influential factor for the good performance is the larger size of the active surface area (compared to Ni and Co), caused by the thick and more corrugated Fe host matrix. The used steel material also contained chromium and manganese (next to silicon and carbon). The Fe:Cr:Ni:Mn ratios were 1:0.16:0.12:0.015 (before deposition)

and 1:0.07:0.18:0.004 (after deposition), respectively. It can be therefore stated that all elements present in the source metal sheet can be detected in the deposited film. It is not clear yet, however, if the observed change in stoichiometric composition before and after deposition, which is the largest for manganese and the lowest for nickel, points to specifics of the reaction and deposition mechanism or is due to statistical variation. Chemical surface properties and bulk properties of the hydroxides were analyzed by XPS, using a Mg K_a X-ray source (excitation energy 1253.6 eV), and EDX. XPS-curves, corresponding to measurements of as-prepared samples are depicted in Figure 3a, b and c by a positive offset (upper curves) and compared to those XPS-measurements obtained after electrochemical treatment (lower curves). The surface region, assessed by these measurements, corresponds to the escape depth (three times of the inelastic mean free paths) of XPS photoelectrons, i.e. the first about 6–9 nm of the films [16]. For nickel and cobalt oxyhydroxides, the XPS core-level signals of as-prepared samples appeared uniformly shifted to higher binding energies by about 3 eV, pointing thereby to low conductivity of the surface region directly after deposition. In the case of Ni, the pronounced satellite structures, following the $2p_{3/2}$ and $2p_{1/2}$ main peaks at binding energies near 865 eV and 880 eV, respectively, point to the presence of the Ni in a higher oxidation state [17]. EDX analysis of a larger sampling volume of the as-prepared sample is not influenced by this low conductivity of the film and shows a pronounced oxygen signal to be assigned to oxygen in the respective oxyhydroxide compound. It is thereby suggested that the film contains already, after deposition and exposure to ambient air, oxidized metal species although the electrodeposition procedure took place under cathodic, i.e. electron supplying conditions. It should be noted that metal oxidation in standard deposition techniques is typically obtained under anodic, i.e. hole-supplying conditions. Similar conclusions are drawn in the case of Co where the corresponding satellite structures near 790 eV and 805 eV, respectively, are typically less prominent but clearly visible [18]. The corresponding electrostatic shift of iron oxyhydroxide remained below 1 eV suggesting higher conductivity of the as-prepared FeO_x. After electrochemical treatment, i.e. potentiostatic anodization at 2 V, all electrostatic shifts vanished and assignment of the respective $2p_{3/2}$ main peaks to documented oxidation states is tentatively possible. According to this analysis, the respective metals appear in an oxidized state, i.e. no Ni(0), Co(0) or Fe(0), respectively, is detected despite the reducing conditions at -10 V. Accordingly, the nickel-derived electrocatalytic film is presumably composed of NiO and $Ni(OH)_2$, the cobalt-derived film may contain CoO as well as $Co(OH)_2$ whereas the iron-derived film may consist of Fe_2O_3 and FeOOH [18]. Accurate deconvolution of the XPS-curves and unambiguous identification of the respective hydroxide and oxide contributions, however, is demanding due to the multitude of theoretical sub-structures as illustrated
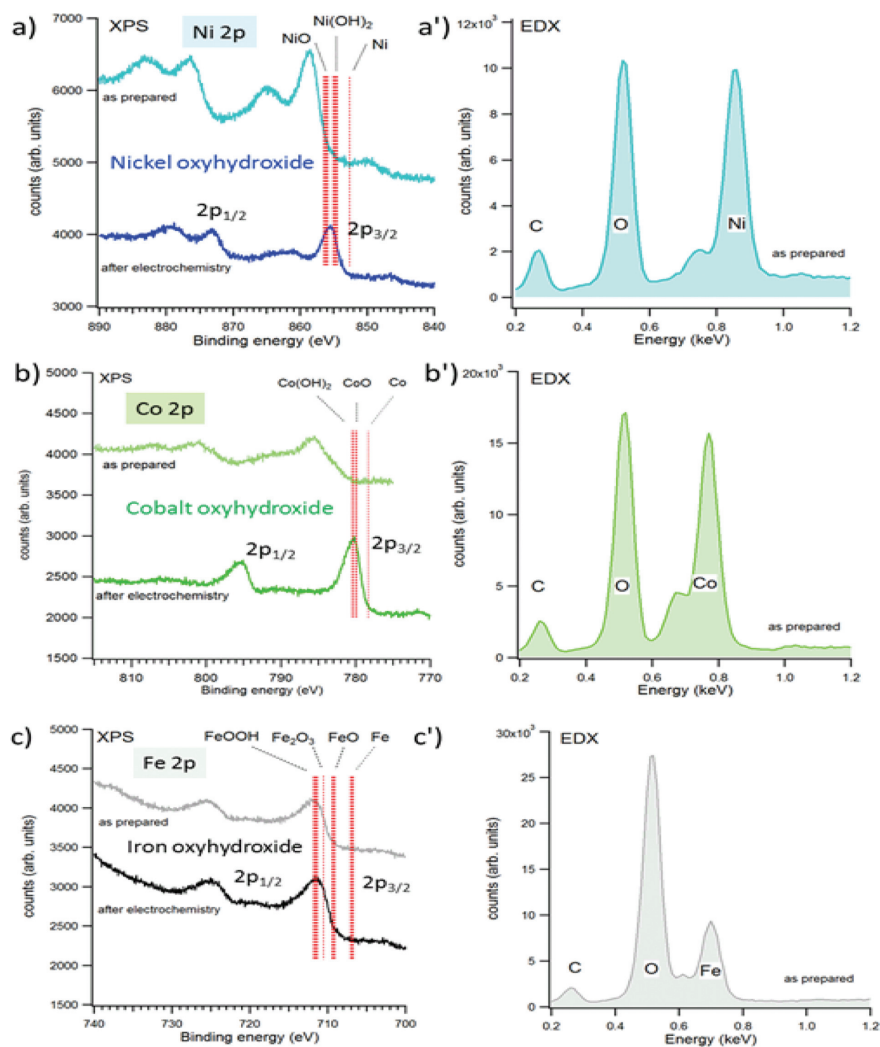
Fig. 3: XPS and EDX analysis of NiO_x (a), CoO_x (b) and FeO_x (c) on Si(111). In (a)–(c) measurements of the respective 2p core-level signals are shown for as-prepared samples (upper curves) and after anodic operation in 0.1 M NaOH, pH13 (lower curves). For as-prepared samples electrostatic charging was observed resulting in a shift of the entire spectrum by about 3 eV (NiO_x and CoO_x) and about 1 V (FeO_x), respectively. EDX analyses of as-prepared samples are additionally shown, probing the chemical composition across a large sampling volume and suggesting the presence of high concentration of oxygen before electrochemical operation as O_2-evolving electrode.

by the following detailed analysis of the nickel-derived electrocatalytic layer. In Figure 4b and c, this detailed analysis of the Ni $2p_{3/2}$ core-level is shown for the as-prepared sample (corrected for the electrostatic shift) and after electrochemical operation. Interpretation of the deposited film as pure nickel hydroxide ($Ni(OH)_2$) is possible due to the high number of sub-structures involved which facilitate a high-quality least-square fit of the measured data. In other words, the presence of NiO cannot be conclusively excluded. For deconvolution of the measured curve, main emission lines (indicated as I_1–I_3), a broad loss structure (dashed line) and three satellite structures (green) were chosen according to established multiplet analysis of $Ni(OH)_2$ based on the work of Grosvenor, Gopta et al. [17, 19]. The results show that nickel hydroxide, after exposure to the ambient, is already present in the as-prepared samples. The changing I_1:I_2:I_3 ratio within the Ni 2p envelope curve (compare Figure 3b and c) indicates commencing structural and chemical modifications upon electrochemical operation.
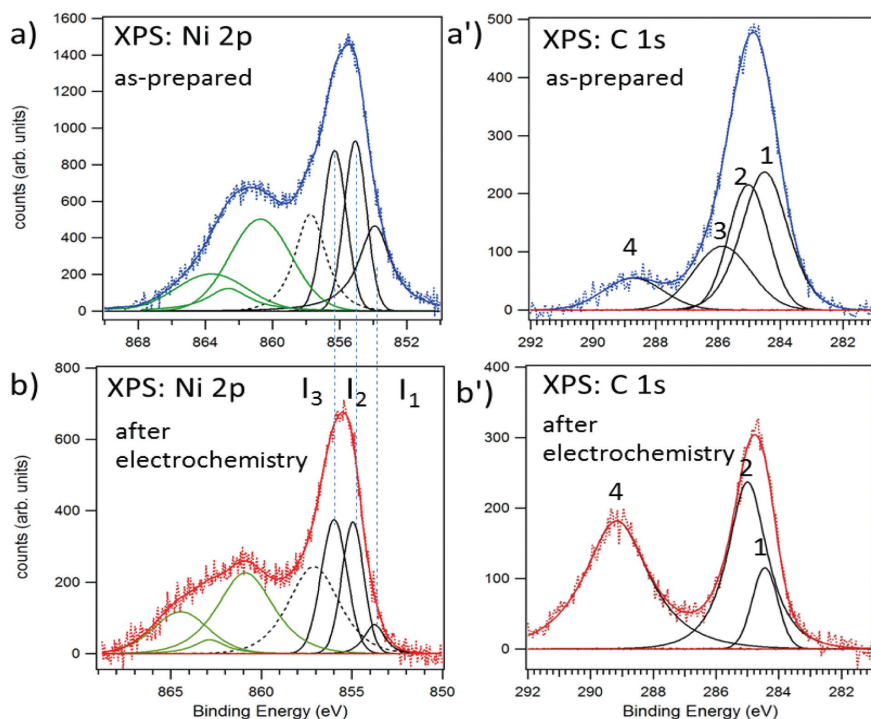

Fig. 4: Detailed XPS analysis of the Ni 2p and C 1s signals of NiO_x before (a) and after electrochemical treatment (b). Main lines and satellite structures of Ni 2p were chosen according to published data (see text). Carbon signals, attributed to different bonding states, are numbered and discussed in the text.

For all samples, carbon was detected by the corresponding XPS C 1s signal (see Figure 4a′ and b′). Beside sp^3-carbon (signal 2 at 285.1 eV), also sp^2-carbon (signal 1 at 284.4 eV) is observed before and after electrochemical operation, indicating that the organic solvent, too, is subject to (electro-)chemical modification upon deposition of the films. A further broad structure in the spectrum of the as-prepared sample (signal 3 at 285.9 eV) is attributed to sp^3-carbon presumably resulting from reaction of the sample with air upon initial exposure to the ambient. This signal is not detected after electrochemistry and it appears likely that this carbon compound is responsible for the low conductivity of the surface region of the as-prepared samples. After electrochemical operation, the concentration of sp^2-carbon has decreased (compare signal 1 in Figure 4a′ and b′) and the emission line around 289 eV (signal 4), to be associated with carboxylic groups, C–OOH, has increased.

According to the results given above, the suggested fabrication route, in fact, results in amorphous transition metal oxyhydroxide layers, applicable to water oxidation reactions in alkaline electrolytes. While the method, particularly by the example of steel, proves its cost-effectiveness upon preparation, also the demand of high electrocatalytic activity has to be addressed in order to ensure cost-effectiveness upon operation. For this purpose overpotentials as low as possible have to be realized. According to Figure 2, these overpotentials still range about 80 mV higher than reported best values such as for iron-modified nickel electrodes (with the composition $Ni_{0.9}Fe_{0.1}O_x$) where the overpotential could be reduced to about 0.336 V [5]. In the following, further optimization of the electro-catalytic activity of nickel-, cobalt- and steel-derived layers is therefore addressed by utilization of FeO_x as core-geometry of a hetero-junction electrode: iron oxyhhydroxide has the lowest electrocatalytic activity of all investigated materials. Its deposition rate, however, is highest, presumably due to its facilitated dissolution in the iodine/acetone solvent, and the resulting FeO_x films are characterized by relatively large surface corrugation and relatively good conductivity. FeO_x therefore is an ideal base-layer onto which materials with higher electrocatalytic activity can be deposited in order to prepare high active-surface-area electrodes.

In order to prepare these hetero-junctions, FeO_x was deposited on FTO for 5 min and subsequently an overlayer of NiO_x, CoO_x and, respectively, a steel-derived oxyhydroxide was formed by further 5 min electrodeposition. Figure 5a depicts the activity of these hetero-junctions in comparison to the corresponding behavior of the single-layer electrodes (characterized by Figure 2). For CoO_x and the steel-derived sample, an increase in charge flow in the region of reversible oxidation and reduction processes indicates a corresponding increase in density of active sites. In the case of NiO_x, a similar increase for the reduction peak is observed while the corresponding oxidation peak is strongly attenuated. This
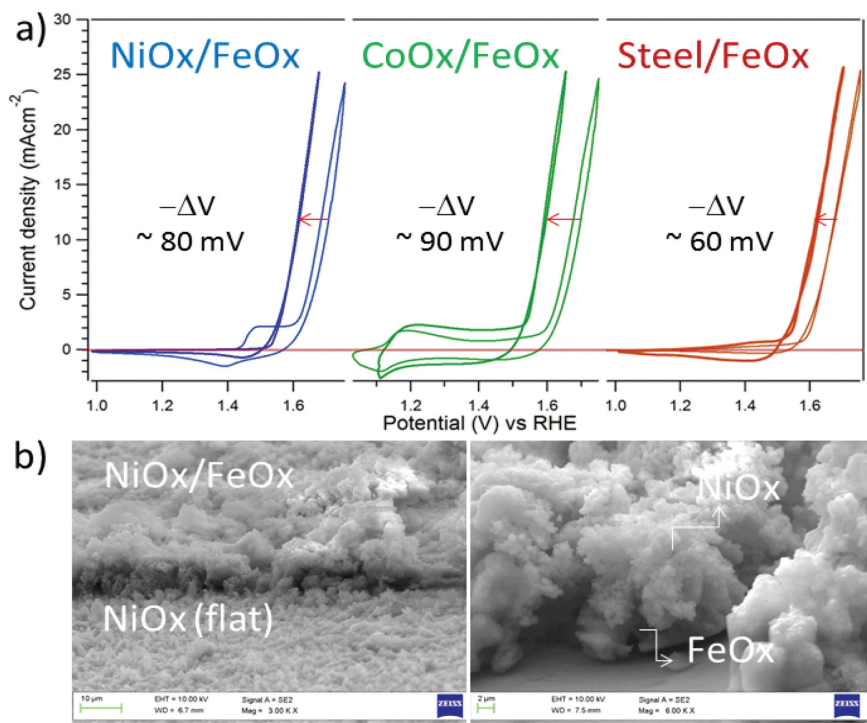
Fig. 5: Increase of the active surface area size of Ni-, Co- and steel-derived electrodes. In (a), the current-voltage behavior of the respective MO_x films (curves with small lime thickness) is compared to the behavior of the corresponding MO_x/FeO_x heterojunctions (larger line thickness). Arrows indicate the achieved shift of the curves towards more negative values as quantified by the indicated numbers. In (b), SEM surface analysis is provided for the NiO_x/FeO_x electrode. Details are discussed in the text.

observation is indicative for irreversible processes due to electrochemical inter-action of the FeO_x base-layer with the NiO_x overlayer. Similar observations were reported earlier for homogeneous NiO_x/FeO_x mixtures but were not yet assigned to specific processes on the molecular level [15]. Most significant is the decrease of the overpotential in the case of NiO_x and CoO_x (80 mV and 90 mV, respectively). The gain in activity for the steel-derived sample amounts to 60 mV. These differ-ences are comprehendible when considering the respective gain in active surface area size. Figure 5b shows that in the case of NiO_x, the thin overlayer reflects the surface morphology of the underlying FeO_x base-layer giving thereby rise to a considerably increased active surface area. This structural improvement can be easily assessed on a smooth silicon support by comparison of two surface regions in Figure 5b, left. In the foreground, NiO_x is directly deposited on silicon. In the

background, the same NiO_x layer is deposited on the FeO_x base-layer (see also magnification in Figure 5b, right). The increase in surface area is clearly visible. Similar results are obtained in the case of the CoO_x/FeO_x junction. In the case of the steel-derived junction, however, the corresponding gain in active surface area size is lower since the steel sample already contained about 90% iron, i.e. the steel/FeO_x junction benefits less from addition of the FeO_x base-layer and the reduction of the overpotential is smaller. Nevertheless, the overpotential for the steel/FeO_x junction (0.38 V) closely approaches the best value obtained for CoO_x/FeO_x (0.34 V). Further improvements, going beyond of the scope of this initial analysis, appear possible either by addition of Co co-catalysts onto the steel-derived overlayer or by further increase of the active surface area size. Since the base-layer material (FeO_x) does merely contribute to the electrocatalytic activity of the junctions, the results of Figure 5 indicate furthermore that the catalytic process of oxygen evolution proceeds preferentially via surface reaction steps (surface catalysis) rather than involving the entire MO_x film (bulk catalysis).

More indication that the bulk is not playing an active role in catalysis is provided when the MO_x films are deposited on an oxidation-sensitive semiconductor. In fact, the cathodic deposition technique allows depositing the oxyhydroxide films onto silicon without risk of silicon self-oxidation. Thereby a functional (and photoactive) junction can be prepared without formation of a passivating SiO_2 interfacial film. Provided that the MO_x film has a pin-hole free structure, inhibiting penetration of the aqueous electrolyte into the layer, such a junction should exhibit, at least, temporary protection and therefore operational stability even in a harsh environment as 0.1 M NaOH. This kind of protection is challenging and is pursued especially in the field of solar water splitting, employing usually very elaborate oxide deposition techniques such as atomic layer deposition (for alkaline media) or polymeric protection (for acidic media) [20–24]. On the other hand, the photocatalytic efficiency of the anode requires that light can reach the photoactive support without strong attenuation and generate sufficiently electron-hole pairs within the penetration depth of light. Optical properties of transition metal oxide films have been analyzed recently in the range of ultra-small thicknesses (0–50 nm) [25]. Preliminary results for the here described oxyhydroxide films with thicknesses between 100 and 200 nm differ considerably from these reports, suggesting lower optical absorbance for NiO_x than for CoO_x (or FeO_x). Consequently, NiO_x was chosen as catalytic protection layer.

In Figure 6a and b, the morphology of NiO_x on n-type Si(111) is depicted on different length scales. The coloring of the layer on the photograph in Figure 6a is due to multiple reflections at the interface of the oxyhydroxide and the support. Here, different colors correspond to different layer thicknesses. Figure 6b demonstrates a nanostructured surface morphology. Areas with different layer
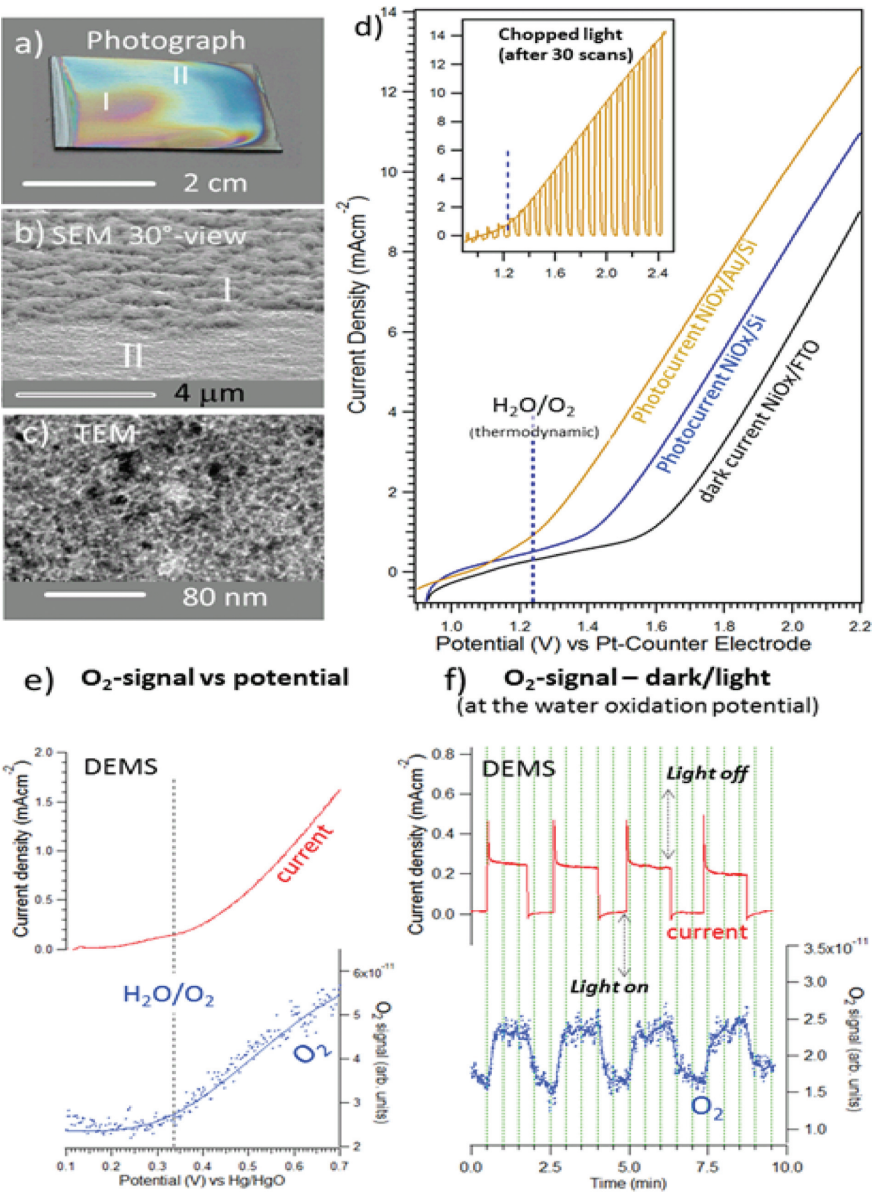
Fig. 6: Topography and electrochemical analysis of $NiO_x/(Au)/Si$. In (a)–(c), photographic and, respectively, microscopic analysis of the NiO_x/Si heterojunction is provided. In (d), the current-voltage behavior of NiO_x/FTO (black curve) is compared to NiO_x on n-Si(111) without (blue curve) and with interfacial Au-layer (orange curve). The inset in (d) shows the performance of the electrode after repeated scans and with intermittent illumination. DEMS analysis is finally provided in (e) and (f), proving the evolution of O_2 by mass spectrometry.

thickness, caused by statistical variation during the deposition process, are indicated by numbers where the thinner area (II) is related to areas with bluish appearance while the thicker area (I) causes more yellowish/reddish appearance. Transmission electron microscopy revealed a dense agglomeration of small amorphous oxyhydroxide sub-units. At some sites continued electron irradiation caused beginning crystallization of these units.

The current-voltage behavior of the NiO_x/Si *junction* (blue curve), in comparison to NiO_x/FTO (black curve), is shown in Figure 6d. An improved onset potential for oxygen evolution by about 150–200 mV is achieved in comparison to NiO_x/FTO. In order to further improve the interfacial charge transfer between NiO_x and silicon, a nanoparticulate Au-interlayer was chemically deposited prior to NiO_x film deposition. The applied chemical deposition method from gold-chloride containing NH_4F solutions also introduces a thin SiO_2 interface which protects silicon against formation of surface/interface states as recently reported [26] resulting in a $NiO_x/Au/SiO_2/Si$ junction (yellow curve).

Thereby, (partial) Fermi-level pinning is reduced and the achievable photovoltage is increased [27]. The presence of this nanoparticulate Au-interlayer results in an additional shift by about 150–200 mV. As a result, photocurrent densities near 1 mA cm^{-2} are detectable directly at the water oxidation potential. The inset in Figure 6d furthermore proves the stability of the prepared junction. Even after 30 scans, the electrode operates with no sign of degradation. The photoactivity was proven by employment of intermittent illumination. Direct evidence for the evolution of oxygen under near-AM1.5 conditions was evidenced by differential electrochemical mass spectroscopy. Figure 6e and f provide, firstly, an O_2-signal concurrently measured during a voltage sweep to 0.7 V vs. Hg/HgO under illumination, and, secondly, during constant potential measurements, slightly above the thermodynamic potential for oxygen evolution (0.4 V vs. Hg/HgO) with intermittent illumination. These results confirm that the observed photocurrent density is almost exclusively of Faradaic nature, i.e. self-oxidation of the support is not detectable. However, after 6–8 h of constant potential operation at 1.8 V RHE, abrupt and progressive degradation was observed. The cause for this instability is attributed to sterical changes in the NiO_x film morphology upon transition to higher oxidation states which facilitate the penetration of the electrolyte towards the silicon interface. This process continues until the $Au/SiO_2/Si$ interface is reached.

These results confirm that the oxyhydroxide films have a structure sufficiently dense to impede penetration of the electrolyte towards the semiconductor interface, i.e. the catalytic reaction for evolution of oxygen proceeds only via surface chemical reaction steps. This finding therefore supports the surface activation strategy outlined above where a highly structured base-layer provides the

geometrical template for a strongly corrugated surface upon which the actual catalytic layer can be deposited with an overall gain in activity. It supports furthermore a complemental strategy where small amounts of additional co-catalysts can be deposited on the surface (e.g. CoO_x) to realize further activity improvements. The bulk material plays only a role when structural changes, upon progressive self-oxidation, open small channels for the electrolyte to penetrate deeper into the bulk.

Based on the observations, outlined above, it is currently assumed that iodides of Ni, Co, and Fe are forming in the acetone/iodine solution by direct dissolution. Upon electron transfer from the cathode, subsequent reactions depend on whether the metal iodide bonding is of monovalent or divalent nature. Ni, Co and Fe, the divalent iodides (NiI_2, CoI_2 and FeI_2, respectively) are forming complexes with the acetone solvent rather than to be reduced to the respective metal. The coordination of these metal centers with the organic molecules, however, remains unresolved so far. A possible coordination, which is tentatively assumed here, is of h^2-type, i.e. the metal ion is bound to both oxygen and the carbonyl carbon of the acetone molecule. Complexes of this type are only meta-stable, i.e. upon exposure to moist air, hydrolysis is considered to cause the observed metal oxidation in the surface film. Carbon, stemming from the metal-organic complexes, is thereby included into the oxidized film, giving rise to the detected C 1s signals as depicted by Figure 4.

Alternatively, the oxide deposition mechanism can be rather similar to a conventional cathodic deposition of oxides in aqueous electrolytes due to the very low stability of transition metal complexes with acetone as ligand. Here, the mechanism is based on the local decrease of H^+-concentration at the cathode side in the course of the cathodic H^+-reduction. This leads to a precipitation of metal hydroxides/oxides in the presence of water either from the acetone solution or water formed by the oxidation of acetone at the anode. Hence, metal oxyhydroxide precipitates are formed directly during the cathodic deposition due to the presence of water and deprotonation occurring at very negative potentials.

In conclusion, a facilitated fabrication route for transition metal oxyhydroxides from solid metal resources as efficient water oxidation catalysts was introduced. Model experiments, using ultra-pure nickel, cobalt and iron sheets, helped devising a suitable iron- and steel-based hetero-junction with low overpotential for the evolution of oxygen. Structural and chemical properties were investigated in detail for nickel oxyhydroxide. The analysis proved a dense and carbon-rich electrocatalytic layer with protection properties for oxidation-sensitive semiconductor supports (silicon).

1 Methods

1.1 Preparation of supports

FTO samples (Solaronix, Suisse, sheet resistance 7 W cm^{-2}) were pre-cleaned by acetone. Silicon samples (n-type Si(111) and Si(100), doping density $N_D \sim 6 \times 10^{15}$, ABC Company, Germany) were pre-cleaned by ethanol and water and chemically etched in dependence of the respective surface orientation: Si(111) was etched in consecutive steps by NH_4F (100 s and 10 min, respectively) and finally dipped in HF (50%) [28]. Si(100) was etched in a 3:1 solution of HF(50%) and Ethanol for 30 s and 10 s with intermediate rinse with water and drying with N_2. Au-nanoparticles were deposited onto silicon supports from a 1:1 mixtures of 10^{-3} M Gold(III) chloride and NH_4F (40%). FTO (3 × 1.5 cm) was used throughout as counter electrode (anode) for deposition of the MO_x films and copper, respectively. Both FTO and silicon (3 × 1.5 cm) were used as supports (cathodes).

1.2 Electrochemical characterization

Oxygen evolution was measured in 0.1 M NaOH, pH13. Current-voltage curves, presented here, were obtained after repeated cycling. The use of 0.1 M concentrated NaOH was necessary due to the observed rapid degradation of FTO supports at higher pH (1 M NaOH, pH14) and the therefore negative influence on the electrochemical characterization of the MO_x films. CO_2-reduction was measured in a phosphate buffered electrolyte (pH7) saturated with CO_2 or, respectively, argon gas. Measurements were carried out in a custom-made electrochemical cell (Figure 1), illuminated, if necessary, from above by a W–I white light source at 100 mW cm^{-2} illumination intensity (MI-150, Dolan-Jenner, Netherlands). For (photo-)current-voltage curves, a scan speed of 20 mV s^{-1} was applied. The potential was controlled using a VSP potentiostat from Biologic, France, SA. Measurements were carried out in a three-electrode arrangement with Pt-counter and Ag/AgCl reference electrode ($E_{Ag/AgCl}$ = 0.198 V vs. RHE). Overpotentials (η) were determined by the difference between the thermodynamic potential for oxygen evolution (E_0 = 1.23 V − 0.059 (pH) − $E_{Ag/AgCl}$ = 0.265 V) and the potential required to reach a current density of 10 mA cm^{-2}. The VSP potentiostat also served for determination of uncompensated IR-drops (with FTO supports) in the used electrolyte. For FTO supports, IR-drop corrected current-voltage curves were derived and depicted in the respective graphs.

1.3 Electron microscopy

Scanning electron microscopy (SEM) and energy dispersive X-ray analysis (EDX) were performed by a Leo 1530 microscope (Zeiss, Germany). For transmission electron microscopy (TEM) a Tecnai G2 20 (FEI, USA) operated at 200 kV was used.

1.4 Photoelectron spectroscopy

X-ray photoelectron spectroscopy (XPS) was employed for analysis of the chemical state of the samples. Assignment of the core-level lines to specific oxidation states was realized using published data [29, 30]. Since the removal of the used O-ring also removed parts of the oxyhydroxide films, the interface of the silicon support could be assessed by XPS, too. To exclude contributions of the FTO support to the O 1s core-level signal (XPS) and to the O K_a X-ray signal (EDX), only (oxide-free) silicon supports were used [28]. Samples were measured directly after film formation (as-deposited) as well as after electrochemical operation in 0.1 M NaOH, pH13, with a linear sweep to 2 V vs. Ag/AgCl and subsequent chronoamperometry at 2 V for 5 min.

1.5 Differential electrochemical mass spectroscopy

Differential electrochemical mass spectroscopy (DEMS) with a Hg/HgO reference electrode was used to analyze the evolving gas in dependence on the applied potential. It was carried out by a custom-made setup equipped with a two-stage vacuum system. The gas was pumped through a first stage (initial pressure 10^{-4} m bar, operational pressure 1–3 $\times$ 10^{-3} m bar) and analyzed by a quadrupole mass spectrometer (initial pressure 10^{-9} m bar, operational pressure about 10^{-7} m bar). DEMS measurements were qualitatively only. A potential drop across the used gas membrane resulted in an increased overpotential.

References

1. Y. V. Kissin, Alkene Polymerization Reactions with Transition Metal Catalysts, in: Studies in surface science and catalysis, 173, Elsevier (2008).

2. H. H. Kung, Transition Metal Oxides: Surface Chemistry and Catalysis, in: Studies in surface science and catalysis, 45, Elsevier (1989).
3. C. A. Grimes, O. K. Varghese, S. Ranjan, Light, Water, Hydrogen, Springer Science+Business Media, LLC (2008).
4. J. B. Gerken, J. G. McAlpin, J. Y. C. Chen, J. M. L. Rigsby, W. H. Casey, R. D. Britt, S. S. Stahl, J. Am. Chem. Soc. **133** (2013) 14431.
5. L. Trotochaud, J. K. Ranney, K. N. Williams, S. W. Boettcher, J. Am. Chem. Soc. **134** (2012) 17253.
6. L. Trotochaud, S. L. Young, J. K. Ranney, S. W. Boettcher, J. Am. Chem. Soc. **136** (2014) 6744.
7. I. Zaharieva, P. Chernev, M. Risch, K. Klingan, M. Kohlhoff, A. Fischer, H. Dau, Energy Environ. Sci. **5** (2012) 7081.
8. M. W. Kanan, D. G. Nocera, Science **321** (2008) 1072.
9. C. A. Kent, J. J. Concepcion, C. J. Dares, D. A. Torelli, A. J. Rieth, A. S. Miller, P. G. Hoertz, T. J. Meyer, J. Am. Chem. Soc. **135** (2013) 8432.
10. C. G. Morales-Guio, L. Liardet, X. Hu, J. Am. Chem. Soc. **138** (2016) 8946.
11. S. Songa, H. Zhanga, X. Maa, Z. Shaoa, R. T. Baker, B. Yi, Int. J. Hydrogen Energy **33** (2008) 4955.
12. M. Carmo, D. L. Fritz, J. Mergel, D. Stolten, Int. J. Hydrogen Energy **38** (2013) 4901.
13. S. Cherevko, S. Geiger, O. Kasian, N. Kulyk, J.-P. Grote, A. Savan, B. R. Shrestha, S. Merzlikin, B. Breitbach, A. Ludwig, Catal. Today **262** (2016) 170.
14. E. Antolini, ACS Catal. **4** (2014) 1426.
15. R. D. L. Smith, M. S. Prévot, R. D. Fagan, Z. Zhang, P. A. Sedach, M. K. J. Siu, S. Trudel, C. P. Berlinguette, Science **340** (2013) 60.
16. M. P. Seah, W. A. Dench, Surf. Interface Anal. **1** (1979) 2.
17. A. P. Grosvenor, M. C. Biesinger, R. St. C. Smart, N. S. McIntyre, Surf. Sci. **600** (2006) 1771.
18. M. C. Biesinger, B. P. Payne, A. P. Grosvenor, L. W. M. Laua, A. R. Gerson, R. St. C. Smart, Appl. Surf. Sci. **257** (2011) 2717.
19. R. P. Gupta, S. K. Sen, Phys. Rev. B **10** (1974) 71.
20. S. Hu, M. R. Shaner, J. A. Beardslee, M. Lichterman, B. S. Brunschwig, N. S. Lewis, Science **344** (2014) 1005.
21. M. J. Kenney, M. Gong, Y. Li, J. Z. Wu, J. Feng, M. Lanza, H. Dai, Science **342** (2013) 836.
22. K. Sun, N. Park, Z. Sun, J. Zhou, J. Wang, X. Pang, S. Shen, S. Y. Noh, Y. Jing, S. Jin, P. K. L. Yua, D. Wang, Energy Environ. Sci. **5** (2012) 7872.
23. Y. Chen, J. D. Prange, S. Dühnen, Y. Park, M. Gunji, C. E. D. Chidsey, P. C. McIntyre, Nat. Mater. **10** (2011) 539.
24. A. Azarpira, Th. Schedel-Niedrig, H.-J. Lewerenz, M. Lublow, Adv. Energ. Mat. **6** (2016) 1502314.
25. L. Trotochaud, Th. J. Mills, S. W. Boettcher, Phys. Chem. Lett. **4** (2013) 931.
26. B. Bouabadi, M. Aggour, H.-J. Lewerenz, M. Lublow, J. Appl. Electrochem. **47** (2017) 457.
27. H. J. Lewerenz, J. Electroanal. Chem. **356** (1993) 121.
28. M. Lublow, T. Stempel, K. Skorupska, A. G. Muñoz, M. Kanis, H. J. Lewerenz, Appl. Phys. Lett. **93** (2008) 062112.
29. J. Chastain, R. C. King Jr. (Eds.), Handbook of X-Ray Photoelectron Spectroscopy, Physical Electronics, Inc., Minnesota, USA (1995).
30. XPS data base of the National Institute of Standards and Technology, NIST, USA.